3D Computer-Assisted Geological Mapping: Testing WinGeol's FaultTrace for semi-automatic structural geological assessment

R. Faber[1] and G. Domej[2]

Received 5 December 2020; accepted 18 January 2021; published 28 February 2021.

WinGeol's FaultTrace is a software tool assisting in semi-automatic structural geological mapping of faults and bedding planes. Digital elevation models – such as, for instance, SRTM or ALOS data – are used in combination with satellite imagery for a first structural geological assessment without the requirement of being at the site. Therefore, it is well suited for inaccessible terrain. Borehole data, geological and seismic profiles can be displayed to support the mapping process. Plane elements can be assigned to single as well as to more complex composite geological structures. Moreover, previously mapped data can be densified by interpolation, which is useful to enhance the mapping quality. The tool aims to provide a virtual environment allowing for fast-track and optimized data generation for 3D geological models. The functionality of FaultTrace is demonstrated in two different case studies: The Richât Structure in Mauritania shows relatively planar fault structures within low-relief topography; the Vineh Structure in Iran shows a complex folding in high mountainous terrain. The studies discuss which structural geological settings let expect a satisfying performance of FaultTrace, and what factors limit the achievement of meaningful results. For the most part, the findings are independent of FaultTrace and, thus, valid for similar software tools.
KEYWORDS: structural geology; faults; bedding planes; 3D semi-automatic computer-assisted mapping; remote sensing; Richât Structure; Karaj Water Conveyance Tunnel.

Citation: Faber, R. and G. Domej (2021), 3D Computer-Assisted Geological Mapping: Testing WinGeol's FaultTrace for semi-automatic structural geological assessment, *Russ. J. Earth. Sci., 21,* ES1007, doi:10.2205/2020ES000757.

1. Introduction

In this publication, we introduce an updated version of the tool FaultTrace^{TM} embedded in the software WinGeol^{TM} by TerraMath ([*Faber and Domej, 2020*]; in the following mentioned as "FaultTrace"). The tool is used to map orientations of faults and bedding planes using digital elevation models (DEM) and referenced aerial and/or satellite imagery; also, conventional geological maps and cross-sections can be assimilated.

Available since 2002 (developed by Faber, 2020; cf. "Data, Imagery and Software Sources"), FaultTrace queues to the list of mapping software using the types of data mentioned above [*Janda et al., 2003*; *Reif et al., 2011*]. During the last two decades, new technologies led to the development of a multitude of new software and ways of data usage, and a full overview, as well as exhaustive comparisons with FaultTrace, would go beyond the scope of this publication. Therefore, only several essential aspects should be highlighted.

Among different online mapping software, Google

[1]TerraMath, Kali Asem, 80152 Buleleng, Indonesia
[2]Università degli Studi di Milano-Bicocca, Dipartimento di Scienze dell'Ambiente e della Terra, Milano, Italy

http://rjes.wdcb.ru/doi/2020ES000757-res.html

Earth is undoubtedly the most widespread. Here, considerable advantages are the ease of use and the accessibility. Inconvenient, though, are the limited control on provided data quality and the dependency on service availability by the provider and Internet connectivity, which might bring the functionality of tools to a sudden end.

The following mapping approaches are to be distinguished:

- manual or automated tools of software performing lineament analysis in 2D only (e.g., ArcMap by Esri, RockWorks by RockWare)
- tools applying the classic three-point-method to calculate orientations of faults and bedding planes in 3D (e.g., GMDE by Richard W. Allmendinger)
- tools focusing on outcrop scale mostly relying on 3D point cloud data from laser scanners or similar sensors (e.g., LIME by the Virtual Outcrop Geology Group)

Considering the critical aspect of lineament analysis in 2D omitting the third dimension, and incorporating the classic three-point-method for plane orientation in 3D, FaultTrace is designed for structural geological mapping of large areas using freely available topographic data such as, for example, ALOS (Advanced Land Observing Satellite) or SRTM (Shuttle Radar Topography Mission) data, and panchromatic, infrared or radar imagery from the Landsat, Sentinel or SPOT (Satellite Pour l'Observation de la Terre) satellites. Also, hyperspectral data (e.g., from the Earth Observing 1 Hyperion Satellite) is supported by FaultTrace.

While generating a 3D geological model, FaultTrace can assist in structural geological assessment of a large area within a short time. Single in-situ measurements of orientation as strike and dip – e.g., from field campaigns – can be incorporated and additional virtual measurements can be added by interpolation in customized intervals. Subsequently, both types of measurements can be grouped and, thus, set in chronological and/or stratigraphic relation to each other. This approach allows for the rapid identification of zones requiring additional mapping efforts to reflect reality by a 3D geological model with a satisfactory level of detail. Here, the advantage is that the user becomes aware of insufficiently mapped zones at an early stage during the process of creating a 3D geological model; i.e., it is not obligatory to loop between a final model state, which is potentially judged unsatisfactory, and the step of refined structural geological mapping.

Although FaultTrace is primarily designed for mapping purposes, it is equally able to visualize borehole data as point-bound depth information, and traditional geological cross-sections as well as seismic profiles as intersections with a DEM. Profiles do not necessarily have to be planar; also, curved intersections can be generated as in the case study of the Vineh Structure in Iran.

As a non-geocoded view option, measurements can be displayed on a Schmidt Net either as an entire set or grouped by subsets. Color scales can be attributed to measurements reflecting the distance to a certain element – e.g., the starting point or the midpoint of a structure – to investigate spatial trends.

To test the performance of FaultTrace, we present two case studies as benchmarks. The Richât Structure in Mauritania challenges the software due to its low-relief topography and shows concentric but relatively planar fault structures. The Vineh Structure in Iran, on the contrary, serves as a straightforward textbook example showing complex fault structures within a variable topographic relief in high mountainous terrain. Both structures are presented shortly hereafter.

1.1. Geological Overview of the Richât Structure

The Richât Structure is located in Central Mauritania in the Adrar Region. Some 30 km northeast of the endpoint of the road connecting Atar and Ouadane, the structure lies in the Sahara Desert, about 125 km away from the city of Chinguetti (Figure 1).

With an average diameter of around 40 km, the "Eye of Africa" displays an almost perfectly concentric structure sequence with a slight elliptical tendency. Located on the Adrar Plateau, the Richât Structure is since the 1980s regularly used by space missions for orientation thanks to its size, regularity and peculiarity compared to its environs [*Scheffers et al.*, 2015]. Over the last decades, various theories concerning the origin of the structure were proposed by different authors. The earliest

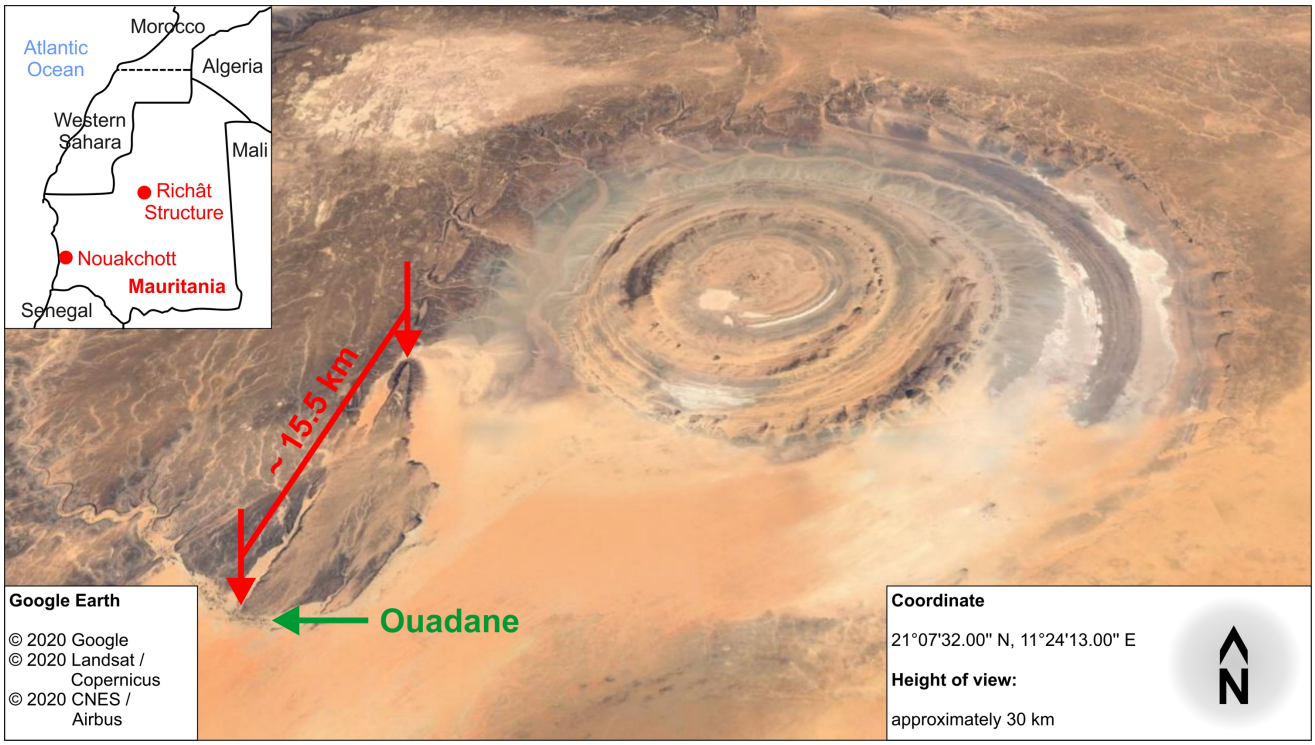

Figure 1. Location of the Richât Structure in Mauritania (background from Google Earth Pro, 2020).

scientific reports date back to the 1930s and 1940s when the structure was discovered and hypothesized to originate from a laccolithic dome having formed an exceptionally symmetric anticline [*Richard-Molard,* 1948]. Twenty years later, *Monod* [1965] suggested consecutive crater-like breaks-ins within the – until then assumed – non-extrusive volcanic setting being responsible for the prominent concentric structures. Shortly thereafter, it was spotted the first time from space by NASA's Gemini IV Project [*Gupta,* 2003], and the possibility of a meteorite impact was discussed [*Barringer,* 1967; *Cailleux et al.,* 1964]. However, due to the lack of evidence proving traces of typical shock metamorphism after such impacts, this theory was rebutted [*Dietz et al.,* 1969; *Fudali,* 1969; *Master and Karfunkel,* 2001]. *Matton et al.* [2005] argued later that volcanic rocks are not found beyond the structure. Nowadays, the prevailing interpretation is that the Richât Structure was formed through doming induced by a large alkaline volcanic intrusion causing uplift and followed by unequally intense erosion of hard and soft rock sequences. Moreover, hydrothermal activity provoked dissolution processes, karstification, and crater-like breakins resulting in the prominent cuesta structures of several meters in height [*Matton,* 2008; *Matton et al.,* 2005; *Matton and Jébrak,* 2014; *Venegas et al.,* 2012]. Dating of the Richât Structure revealed Late Proterozoic to Ordovician ages [*Netto et al.,* 1992; *Poupeau et al.,* 1996]. The traces of human beings are proven to be solely terrestrial – in contrast to many "creative" extraterrestrial theories attempting to explain the origin of the structure. A multitude of Acheulian artifacts dating to the Neolithic (corresponding to the Late Pleistocene) is described by *Sao et al.* [2008].

Due to the exceptional variety of structural geological features within the igneous, metamorphic and sedimentary units of rock, the Richât Structure offers a wide range of possibilities to test the tool FaultTrace of the software WinGeol.

1.2. Geological Overview of the Vineh Structure

The Vineh Structure is located in Northern Iran in the Alborz Province. Following Road 59 from Karaj in the direction to Chalus, the structure lies east of the village of Vineh, about 25 km away from

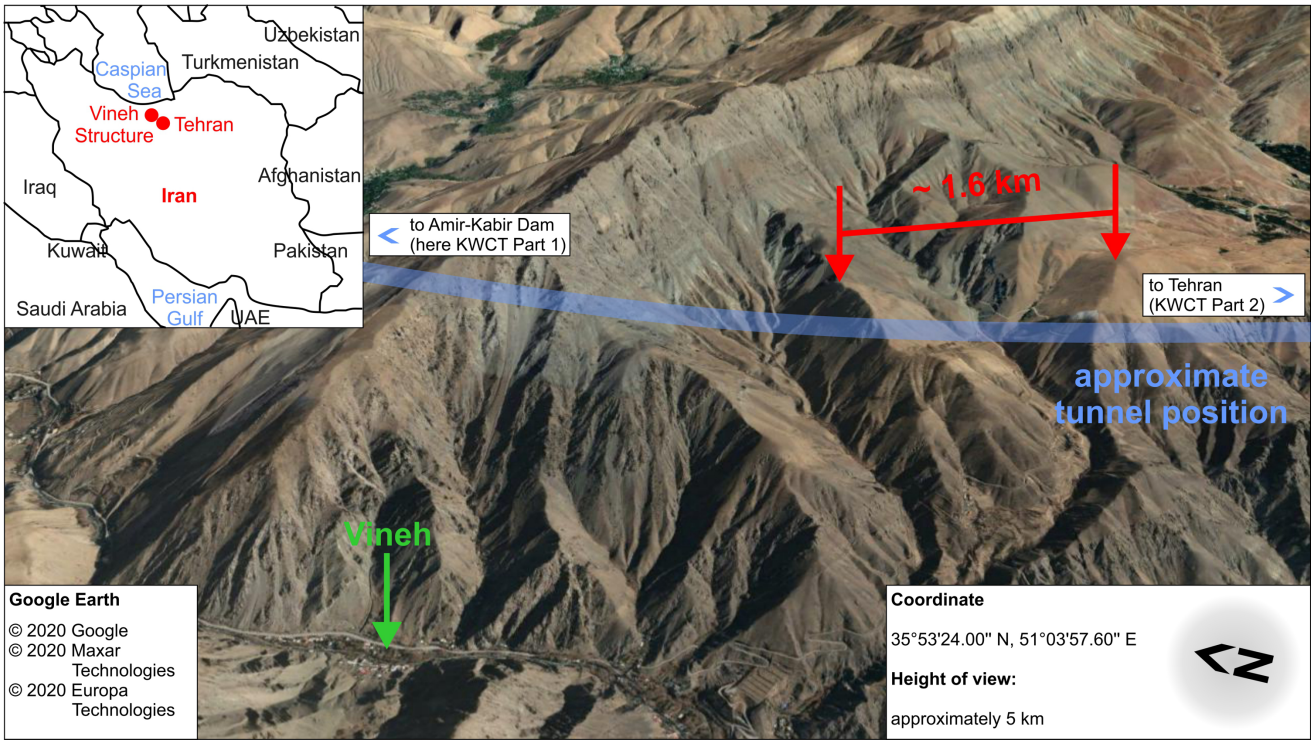

Figure 2. Location of the Vineh Structure in Iran (background from Google Earth Pro, 2020). The position of the Karaj Water Conveyance Tunnel (KWCT) is roughly approximate.

the country's capital Tehran (Figure 2).

Although not being known in the literature under the given name, the Vineh Structure is called as such in this publication for simplification and due to its close vicinity to the village of Vineh. The prominent colorful and multilayered outcropping unit shown in Figure 2 belongs to the Karaj Formation and lies within the Alborz Mountains. The formation is moderately to heavily faulted and consists of Middle to Late Eocene submarine rock sequences and Oligocene intrusive bodies [*Hassanpour et al.*, 2010 and 2014].

Significant interest in this particular section of the Alborz Mountains had arisen since the 1920s when water resource management began in order to satisfy the demand of the steadily growing metropolitan area of Tehran. Until then, a channel branching off the Karaj River delivered freshwater to Tehran but soon could not satisfy the demands. Within the following 30 years, a comprehensive plan including three reservoirs and the tapping of the Tehran Aquifer was established. Between the 1960s and the 1980s, the three dams of Lar, Latyan and Amir-Kabir were constructed, of which the latter nowadays retains the Karaj River on more than 10 km [*Bagheri et al.*, 2006; *Karamouz et al.*, 2001]. Flowing southwards as one of the main drains of the Alborz Mountains and ultimately discharging into the endorheic Namak Lake in Central Iran, the Karaj River passes just west of the Vineh Structure through the valley hosting the Road 59.

After the turn of the millennium, the Karaj Formation became a focus of interest again, as the Karaj Water Conveyance Tunnel (KWCT) was to be drilled in two segments (Parts 1 and 2; Figure 2) in a curve through the mountain ridge on a total length of 30 km in order to tap the Amir-Kabir Dam and deliver around 16 m^3/s of freshwater through a pipe with a diameter of roughly 4.5 m to the eastern suburbs of Tehran. Although designed to spare the two major thrust faults in the region (i.e., the Purkan-Vardij Fault and the North Tehran Fault), the KWCT crosses though their influence zone twice: first, approximately at the middle of Part 1 and, second, around the last 3 km of Part 2. The first area coincides with the Vineh Structure in which the KWCT passes in a curve some 1.5 km inside the mountain ridge [*Has-*

sanpour et al., 2010 and 2014; *Morsali et al.,* 2017 and 2018].

Detailed technical studies documenting the encountered geological sequences of igneous and sedimentary units of rock along the two KWCT segments (Part 1: 13.2 km from the dam southwards to the junction; Part 2: 15.8 km from the junction southwestwards to Tehran) are published by several authors [*Farhadian et al.,* 2016 and 2017; *Ghiasi et al.,* 2012; *Hassanpour et al.,* 2010 and 2014; *Jalali,* 2018; *Khanlari et al.,* 2012; *Khanlari and Ghaderi-Meybodi,* 2011 and 2013; *Mirahmadi et al.,* 2016; *Morsali et al.,* 2017 and 2018; *Soleiman-Dehkordi et al.,* 2015]. Mentioned structural geological features are remapped with the tool FaultTrace of the software WinGeol to test the software performance.

2. Data

The DEM used in this publication are the ALOS PALSAR (ALOS Phased Array type L-band Synthetic Aperture Radar) Model for the Vineh Structure and the ALOS World 3D Model for the Richât Structure. Additionally, we used multispectral Landsat ETM+ (Landsat Enhanced Thematic Mapper Plus) and Sentinel-2 Satellite Imagery (Table 1).

A crucial point for geological mapping in 3D is the accuracy of DEM, which is extensively discussed by several authors [e.g., *Alganci et al.,* 2018; *Bayik et al.,* 2018; *Julzarika,* 2015; *Mukul et al.,* 2017; *Rodrigues et al.,* 2001]; vertical errors are commonly given with respect to reference points (i.e., the so-called "ground truth") or to a reference DEM. It is important to note that accuracies do not solely depend on the sensor quality but may also differ according to the nature of the terrain and the land cover [e.g., *Mukul et al.,* 2017]. Usually, absolute vertical accuracies are guaranteed by the data providers; however, different authors obtained better accuracies for different case studies (Table 1).

One major factor influencing the accuracy of DEM is the vegetation cover. Especially when the vegetation cover is thick, DEM are more prone to inaccuracy due to different interactions of radar waves with the encountered surfaces [*Santillan and Makinano-Santillan,* 2016]. However, in the case studies presented in this publication, the aspect of vegetation cover can be neglected as both locations are characterized by arid climate conditions and, thus, very sparse vegetation.

As a matter of course, accuracies indicated by data providers (Table 1) tend to reflect less satisfactory results with a wider range of possible error, whereas studies conducted by different authors using the provided data in distinct locations and within particular conditions of applications might deliver much better accuracies – i.e., lower error ranges – compared to those given by the providers.

Considering the above-mentioned limitations on DEM accuracy, and the fact that greater altitude variations strongly impact results (e.g., lower precision by *Farr et al.* [2007] and *Mukul et al.* [2017] for high mountainous terrain; e.g., lower precision by *Farr et al.* [2007] for smooth sandy surfaces), we estimated the structural geological features of the two case studies to be mapped with different precision. For the Vineh Structure, the higher quality ALOS PALSAR DEM was used in a strongly variable relief environment, whereas for the Richât Structure, the lower quality ALOS World 3D DEM was applied in a topographically very flat area with less prominent altitude differences entailing a much higher signal-to-noise ratio. Relying on data from providers, the two case studies represent the lowest level of precision conditioned by the data accuracy. This, however, does not curtail the performance of FaultTrace.

3. Methodology and Software Functionality

FaultTrace offers two procedures for assessing plane structural geological features such as, for example, faults and bedding planes (Figure 3). It is important to note that these features meet the definition of "geological faces" with various degrees of curvature and, therefore, orientated plane elements can only be attributed to them as tangential planes in particular locations.

The primary mapping procedure is a further development of 2D lineament mapping, as this method is still widely used [e.g., *Abdullah et al.,* 2013; *Akram et al.,* 2019; *Alshayef et al.,* 2017; *Elhag and Alshamsi,* 2019] and a well-accepted standard in structural geology. After importing a high-resolution DEM and – if available – additional satellite imagery, visually identified lineaments [*O'Leary et al.,* 1976] are traced manually as

Table 1. Datasets of digital elevation models (DEM) and satellite imagery with their resolutions and vertical accuracies. Datasets marked with an asterisk (*) were used for testing FaultTrace. Source details are given in "Data, Imagery and Software Sources"

Type	Dataset	Resolution (and vertical accuracy) by the provider	Vertical accuracy by different authors
DEM	ALOS PALSAR*	12.5m (±5.5 m)	0.78–4.57 m [*Shawky et al.,* 2019], 5.5 m [*Chu and Lindenschmidt,* 2017]
DEM	ALOS World 3D*	30.0 m (±5 m)	5.68 m [*Santillan and Makinano-Santillan,* 2016]
DEM	SRTM	30.0 m (±16 m)	5.94 m [*Elkhrachy,* 2018], 8.28 m [*Santillan and Makinano-Santillan,* 2016]
satellite imagery	Sentinel-2*	10.0 m (-)	(no vertical component)
satellite imagery	Landsat ETM+*	30.0 m (-)	(no vertical component)

polylines connecting multiple points. One polyline traces one lineament; it consists of several segments called "elements". Azimuths (in degrees clockwise from north) with temporary dips of 90°(from the horizontal) are automatically assigned to each element center. From these elements approximating the lineament in 2D, plane elements in 3D are created, which intersect the DEM as so-called "trace lines", still having a perfectly vertical dip. Plane element centers are then automatically shifted in vertical direction to the trace line. In the next step, orientations of each plane element are manually corrected through variation of the dip, rotation of the azimuth around the plane element center, translation of the plane element center and/or adjustment of the length of the plane element. The criterion of optimal orientation is the coincidence of the visually identified lineament and the trace line of the plane element.

Alternatively, a procedure based on the three-point-method (as described by *Allmendinger,*[2018]) can be used to define plane elements in 3D without mapping lineaments. Here, three points belonging to the same visually identified structural geological feature are directly placed on the DEM. The orientation of the plane element defined by these three points is then given likewise as azimuth and dip. Even though representing a method in 3D from the outset, plane element correction is in the most cases necessary and achieved in the same way as described above.

Independently of the technique of plane element creation, it is then possible to interpolate a series of virtual plane elements between two or more mapped and corrected plane elements of the same structural geological feature. The interpolation procedure uses Hermite's Formula (as described by *Spitzbart,* [1960]) to create a spline between two mapped and corrected plane element centers in top view – i.e., on a projection to the horizontal. The intersection of the strikes of the plane elements is used as pole for the spline during the interpolation of additional azimuth-dip-pairs in between. Interpolation intervals along the spline can be adjusted as needed. However, as the mapped and corrected plane element centers usually have a vertical offset in reality, the spline is transposed accordingly into the 3D space using simple trigonometry, and altitudes are assigned to each interval step. Respective dips at each interval step are interpolated linearly, taking into account the difference between the dips of the mapped and corrected plane elements as well as the number of intervals. Trace lines of virtual plane elements are likewise shown as for mapped and corrected plane elements. However, centers of virtual plane elements are not necessarily located on their trace lines as they lie on the tilted spline created with Hermite's Formula.

In the next section, we present a comparative mapping strategy. Available literature was evaluated with regard to structural geological features such as prominent shapes, dykes, faults and fault systems, general and conjugated fracture sets, typical volcanic con- and discordances, and bedding sequences. For both the Richât Structure and the Vineh Structure, the identified features were then

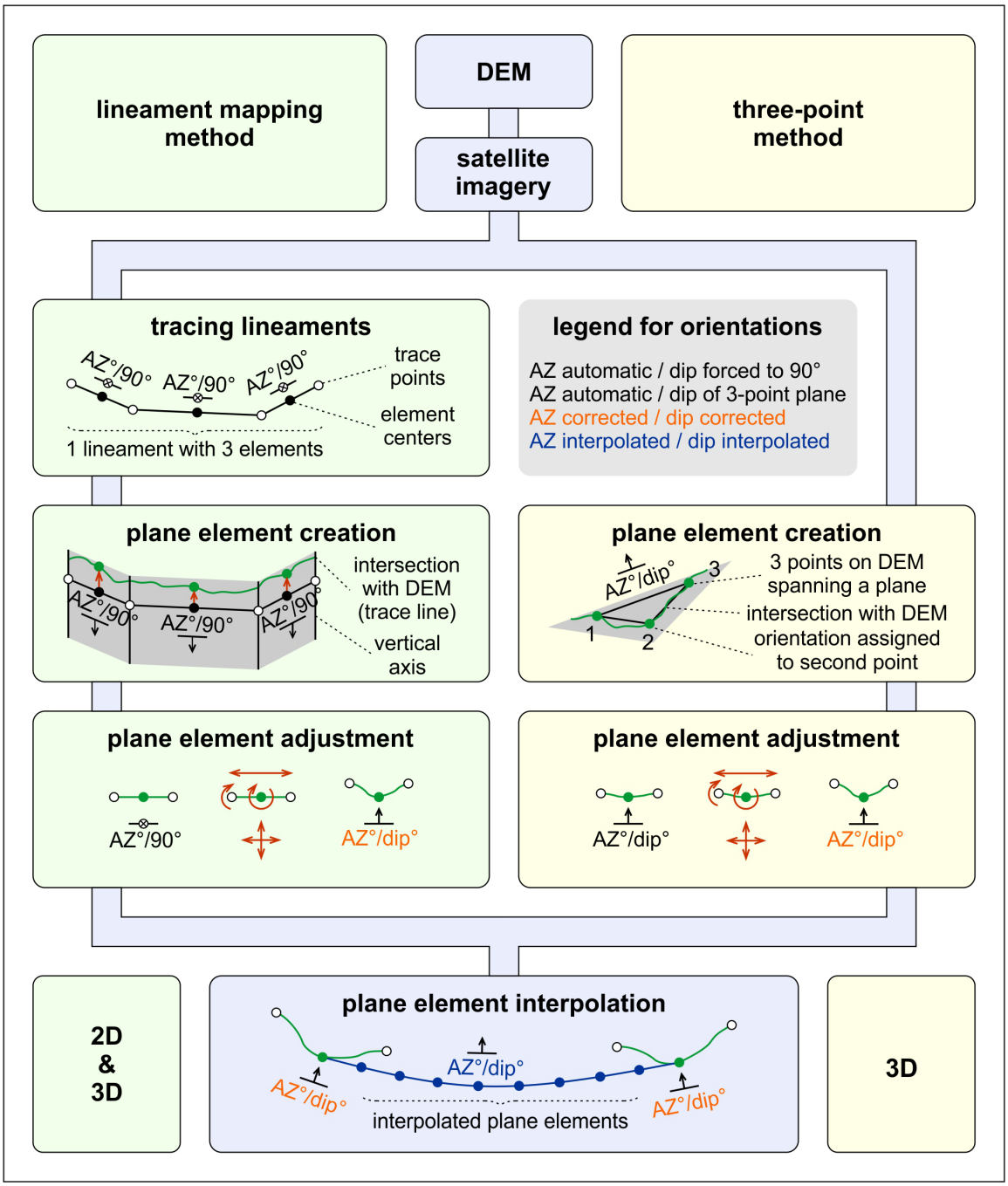

Figure 3. Mapping procedure of FaultTrace via the lineament mapping method in 2D and 3D or the three-point-method in 3D.

remapped with FaultTrace in order to test the qualitative mapping performance of the software tool by comparing the obtained results to the observations given in the literature. Correspondences and misfits obtained by FaultTrace are discussed in the next section.

4. Results of Mapping with FaultTrace

Structural geological features mentioned in the literature are listed in Table 2 and Table 3 for the Richât Structure and the Vineh Structure, together with the respective describing authors. Running

Table 2. Structural geological features of the Richât Structure according to different authors. Orientations are given as strike (in degrees from north eastwards) and dip (in degrees from the horizontal)

No.	Type of feature	Observation in literature	Author(s)
R_S1	shapes	elliptical shape stretched in NE–SW (axis ratio 0.87–0.88), diameter of 40–50 km	[*Matton,* 2008], [*Matton et al.,* 2005], [*Matton and Jébrak,* 2014]
R_D1	dykes	concentric dykes with reliefs of 20–30 m, dipping outwards with 10–20° (up to 35° in the center)	[*Matton,* 2008], [*Matton et al.,* 2005], [*Matton and Jébrak,* 2014], [*Woolley,* 2001]
R_D2	dykes	2 gabbro dykes at 3 km (20 m thick) and 7–8 km (50 m thick) from the center	[*Deynoux & Trompette,* 1971], [*Matton,* 2008], [*Matton et al.,* 2005], [*Matton and Jébrak* 2014], [*Poupeau et al.* 1996]
R_D3	dykes	32 carbonatite plane dykes (including sills), strikes of 15–30°, lengths of up to 300 m (1–4 m thick)	[*Matton,* 2008], [*Matton et al.,* 2005], [*Matton and Jébrak,* 2014], [*Netto et al.,* 1992], [*Poupeau et al.,* 1996]
R_F1	faults	fault system I, strikes of 10–20° (chronologically older)	[*Netto et al.,* 1992], [*Poupeau et al.,* 1996]
R_F2	faults	fault system II, strikes of 70–90° (chronologically younger)	[*Netto et al.,* 1992], [*Poupeau et al.,* 1996]
R_f1	fractures	brittle fracture system I parallel to fault system I (R_F1), dextral, some vertical offset	[*Matton,* 2008], [*Matton et al.,* 2005]
R_f2	fractures	brittle fracture system II parallel to fault system II (R_F2), sinistral	[*Matton,* 2008], [*Matton et al.,* 2005]
R_f3	fractures	concentric fracture system in the center	[*Deynoux & Trompette,* 1971], [*Matton,* 2008], [*Matton and Jébrak,* 2014]
R_I1	intersections	fault system II (R_F2) intersecting fault system I (R_F1), stress regime possibly responsible for elliptical shape (R_S1)	[*Netto et al.,* 1992], [*Poupeau et al.,* 1996]
R_I2	intersections	fault system I (R_F1) intersecting gabbro dykes (R_D2) in the NE	[*Matton,* 2008], [*Matton et al.,* 2005]
R_I3	intersections	carbonatite dykes (R_D3) intersecting gabbro dykes (R_D2) in the SW	[*Matton,* 2008], [*Matton et al.,* 2005]
R_I4	intersections	brittle fracture system II (R_f2) intersecting cuestas (R_V2) in the W	[*Matton,* 2008], [*Matton et al.,* 2005]
R_V1	volcanism	laccolithic uplift forming a dome structure (anticline)	[*Richard-Molard,* 1949]
R_V2	volcanism	multiple cuestas (after crater break-ins)	[*Monod,* 1965]
R_V3	volcanism	2 maar systems, eruptive rock dipping towards the center with 15–27°, in the NE and the SW (Sabkha filling the SW crater)	[*Matton,* 2008], [*Matton and Jébrak,* 2014]
R_B1	bedding	mega-breccia in the center, diameter of 3 km (up to 40 m tick)	[*Matton et al.,* 2005]

Table 3. Structural geological features of the Vineh Structure and its surroundings according to different authors. Orientations are given as strike (in wind directions)

No.	Type of feature	Observation in literature	Author(s)
V_F1	faults	fault system of Purkan-Vardij Fault, strikes of NW–SE in this area	[*Hassanpour et al.*, 2010 and 2014], [*Rajabi et al.*, 2012]
V_F2	faults	fault system of Northern Tehran Fault, strikes E–W generally	[*Hassanpour et al.*, 2010 and 2014], [*Rajabi et al.*, 2012]
V_f1	fractures	brittle fracture system conjugated to fault system of Purkan-Vardij Fault (F1), shear zones (10–50 m thick), in the middle of KWCT (Part 1)	[*Hassanpour et al.*, 2010 and 2014]
V_f2	fractures	joint sets along KWCT (Parts 1 and 2)	[*Hassanpour et al.*, 2010]
V_I1	intersections	KWCT intersecting fault system of Purkan-Vardij Fault (F1) with 70° in the middle of KWCT (Part 1)	[*Jalali*, 2018], [*Khanlari et al.*, 2012], [*Khanlari and Ghaderi-Meybodi*, 2011 and 2013]
V_B1	bedding	Syncline of Azgilak	[*Hassanpour et al.*, 2010 and 2014]
V_B2	bedding	Anticline of Vardij	[*Hassanpour et al.*, 2010 and 2014]

numbers correspond to those in the descriptive text as well as in Figure 4 and Figure 5.

Besides, we also mapped distinct structural geological features which are not mentioned in the evaluated literature but which are outstanding due to their noticeable appearance on the overlay of satellite imagery on the DEM.

4.1. Mapping of the Richât Structure

Figure 4 provides different views of the Richât Structure and simultaneously represents examples of possible visualization and analysis modes in FaultTrace.

The first sub-figure (tile a) shows the entire structure with plane element orientations along the two main axes; both are extracted as cross-sections (tile d). The longer axis indeed orientates north-northeast – south-southwest, and the shorter one is roughly orthogonal to it. Considering the length difference of both axes measured with respect to the concentric dykes, the axis ratio is 0.9 and clearly depicts an elliptic structure (R_S1). Although disturbed in some sections, the concentric dykes generally run around the center and reach topographic elevations of several tens of meters above the flatter environs. Orientations of plane elements along the two main axes dip outwards with increasing dips towards the center, reaching their maxima at around 5–8 km from the center (R_D1). Dips appear, however, flatter as indicated in the literature. Respective strikes are roughly orthogonal to the main axes. It should be noted that for the Richât Structure all 3D views (tiles a and b) as well as the cross-section (tile d) show topographies with ten-fold exaggerated vertical axes due to the prevalent flat terrain. Visually, dips adjust automatically to the chosen exaggeration factor, but keep their true numeric value.

Particular attention is paid to the gabbro and carbonatite dykes, as they are mentioned to appear discordantly to the surrounding structures due to their intrusive genesis. The gabbro dykes are assumed to emerge as significant color contrast concentrically at around 3 and 8 km from the center (R_D2). Here, the option of color band modification, and hence the creation of false-color imagery, is a useful asset in FaultTrace. The remapping of the thicknesses of these dykes – i.e., of 20 and 50 m, respectively – was, however, limited due to DEM and satellite imagery resolutions in the same range of accuracy. The series of carbonatite dykes and sills in the southwestern part of the Richât Struc-

ture are too small to be mapped due to their shortness and thinness of some meters only (R_D3).

Overall, the Richât Structure is characterized by two structural geological settings: (i) the above described volcanogenic elliptical dyke structures, which are probably a result of multiple crater breakins resulting in cuestas (R_V2) followed by erosion; (ii) the regional tectonic setting dominated by two fault systems (R_F1 and R_F2) and their respective parallel brittle fracture systems (R_f1 and R_f2). The main axes of the elliptical dyke structures roughly align with the two fault systems.

One asset of FaultTrace to analyze orientations of plane elements qualitatively and quantitatively are lineament rose statistics that can be performed either for customized sub-areas or the entire mapped area. In each lineament rose, the radii of the colored segments are proportional to the sum of the lengths of all concerned lineaments. The Richât Structure is divided into 20 sub-areas (tile e). Despite some outliers, it is apparent that in all lineament roses at least one of the two fault systems (R_F1 and/or R_F2) and one of the two associated brittle fracture systems (R_f1 and/or R_f2) are dominant, showing strikes in north-northeast – south-southwest and/or east–west respectively. Thereto compared, in lineament roses of sub-areas covering only the inner areas of the Richât Structure, segments also reveal much shorter lineaments with strikes distributed across all directions; they are, thus, interpreted to represent the concentric fracture system (R_f3). Likewise, the lineament rose for the entire mapped area (tile f) indicates the dominance of the two fault systems, which are believed to have first created favorable preconditions for crust-thinning and volcanism at their intersection (R_I1) and secondly caused the elliptical form due to the persistent stress regime.

The brittle fracture system I seems indeed to be primarily dextral (R_f1; tile a), but the mentioned vertical offsets could not be remapped. The brittle fracture system II is mentioned to be sinistral (R_f2); a zoom on the area, which is identified by the lineament rose statistics to contain a considerable amount of lineaments of associated strikes, seems, however, to contain both sinistral as well as dextral lateral offsets (tiles b and c). Some other prominent remapped features are the intersections of the fault system I with the gabbro dykes (R_I2; tile a) and the one of the brittle fracture system II with the cuestas (R_I4; tile d); the mentioned intersection of carbonatite and gabbro dykes (R_I3; tile a) cannot be remapped due to resolution issues. Of the three discordant volcanic intrusions, only one is easy to identify – although only from the top without the possibility of verifying its dip: the greater of the two maar systems, as it is said to be filled by a Sabkha (Arabic for: evaporitic sand flat; R_V3; tile a) and, therefore, emerging as significant color contrast. The second maar system is much smaller and similar to a small laccolithic intrusion appearing as anticline (R_V1; tile a); it is remapped with reservation. The mega-breccia extends indeed over 3–4 km in the center of the Richât Structure, but its depth could not be evaluated (R_B1; tile a).

4.2. Mapping of the Vineh Structure

Compared to the case study of the Richât Structure in Mauritania, the Vineh Structure in Iran is different due to its high topographic relief and the fact that stratigraphic sequences are much more variable as Figure 2 and Figure 5a let assume from colorful outcropping lithological units. Therefore, faults as well as bedding planes were remapped with FaultTrace to exemplify its applicability for both types of associated lineaments and plane elements. Moreover, we demonstrate the visualization of given data as additional information for 3D structural geological assessments; in this case, a geologic cross-section along the first part of the KWCT (Sadeghi, 2010; cf. Acknowledgments) was positioned along the curved tunnel profile and intersected with the DEM.

Figure 5 provides different views of the Vineh Structure and its environs in 2D and 3D, showing in total lineament orientations and plane elements of 19 bedding planes (0–18; marked in green) and 26 faults (0–25; marked in red). Fault 21 is located outside of the area of interest.

The first sub-figure (tile a) shows the entire structure – i.e., the mountain ridge close to the main curve of the KWCT – and its environs with lineament orientations of bedding planes and faults. The Amir-Kabir Dam is located just north of bedding 0; the second part of the KWCT is directly adjacent to the end of the first one close to bedding 16 and continues to the outskirts of Western Tehran (tile d). Following the method of lineament

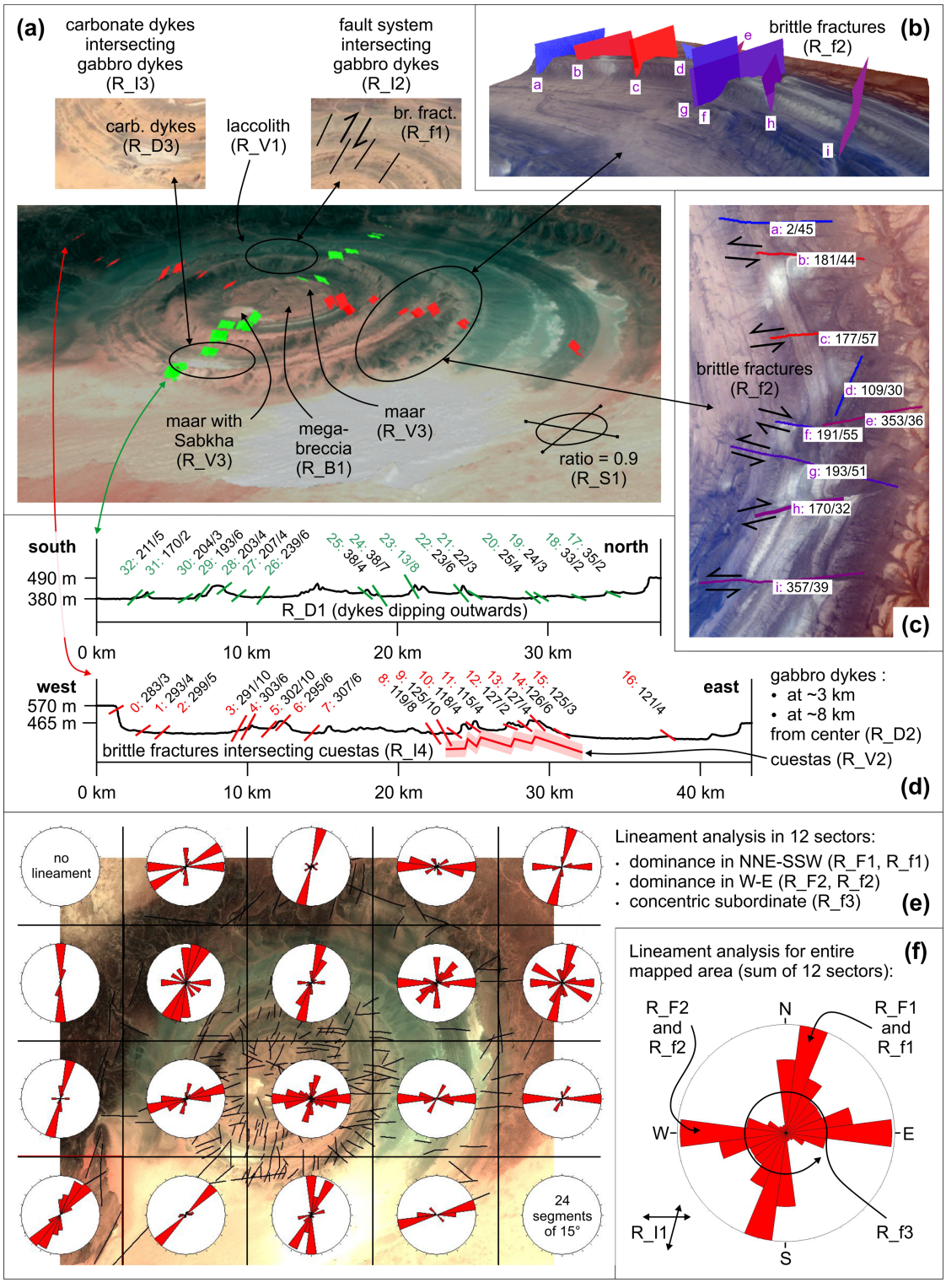

Figure 4. Mapping of the Richât Structure with FaultTrace: (a) 3D view showing plane element orientations along the two main axes; (b, c) 3D and 2D views showing the heavily sheared zone in the eastern part; (d) 2D view showing the cross-sections along the two main axes; (e) 2D view showing distributions of lineament orientations per sector; (f) lineament rose showing the overall distribution of lineament orientations. All vertical axes are ten-fold exaggerated (a, b, d); lateral scale relations are given in the cross-sections (d).

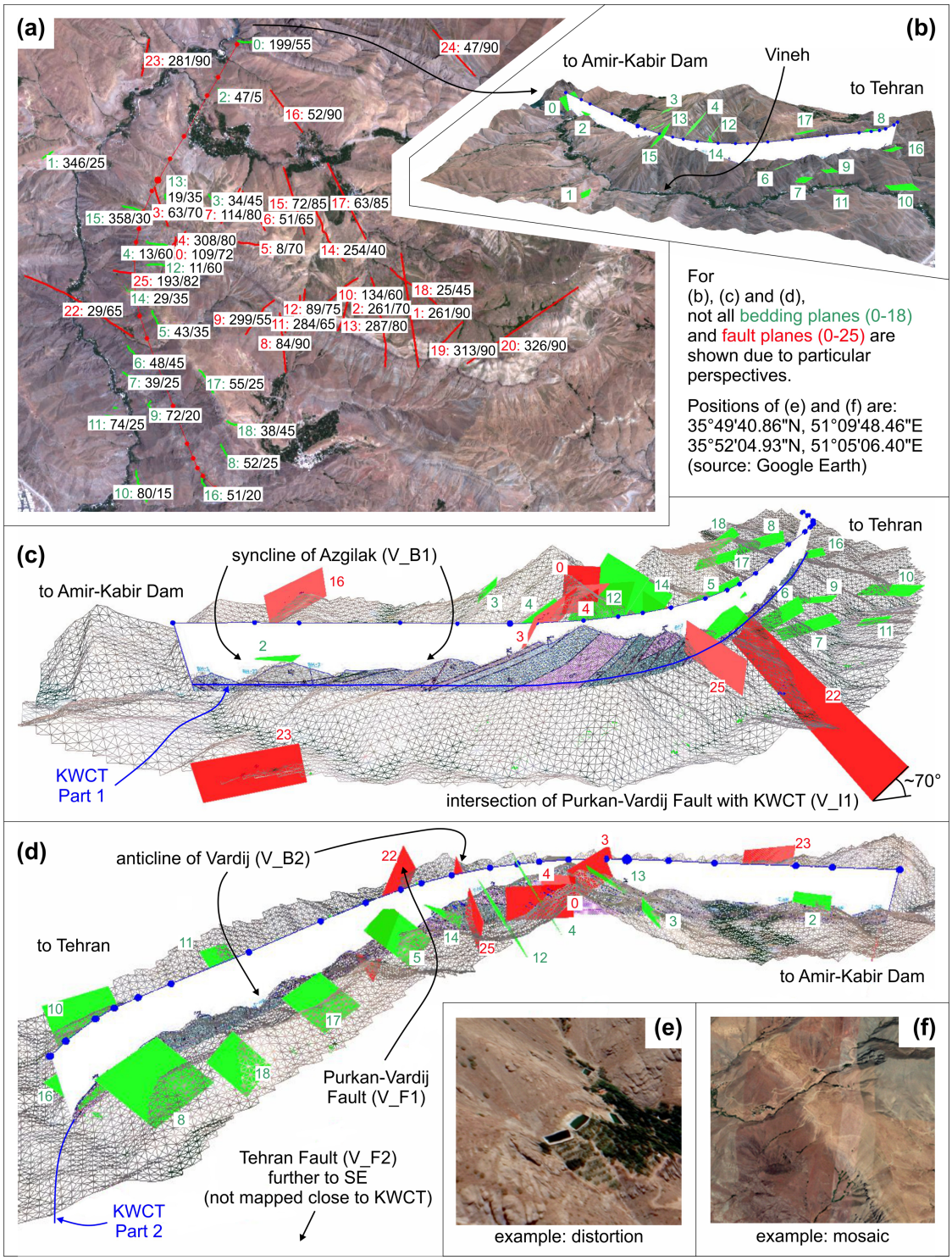

Figure 5. Mapping of the Vineh Structure with FaultTrace: (a) 2D view showing distributions of lineament orientations of bedding and fault planes; (b) 3D view showing bedding plane elements; (c, d) 3D views showing bedding and fault plane elements; (e, f) examples of distortion effects and mosaic tiles in Google Earth (imagery from Google Earth Pro, 2020). The cross-section inserted in (c) and (d) is provided by Sadeghi (2010; cf. Acknowledgments); it shows only the first part of the Karaj Water Conveyance Tunnel (KWCT).

mapping (Figure 3), those were mapped in a first stage for bedding planes and faults in 2D before adjusting the respective azimuths and dips in order to position the 3D plane elements correctly with respect to their trace lines. Here, the aspect of the resolution of the DEM and the used satellite imagery is of particular importance and must be considered while mapping. Especially when lithological units are relatively thin, and when their thickness is equal to or smaller than the resolution of the DEM and/or the draped satellite imagery, it becomes more difficult as no significant color contrast can be identified. To overcome this difficulty, we resorted, on the one hand, to cross-sectional information (Sadeghi, 2010; cf. Acknowledgments; tile c) which allowed for the extraction of bedding plane orientations in 3D, and on the other hand, to satellite imagery from Google Earth Pro, which was used in parallel to FaultTrace to position bedding plane elements along the KWCT (tile b). Attention has to be paid to the fact that Google Earth Pro provides satellite imagery, which has – in most cases – a higher resolution than SRTM data; the underlying DEM of Google Earth Pro is, however, usually less accurate compared to DEM data such as the one used in this study. Common effects in Google Earth Pro are, thus, different forms of distortions which are straightforward to identify, when artificial horizontal structures in the area of interest could serve as a reference. For instance, the inclined surfaces of standing water bodies (tile e) clearly prove a misfit between the used DEM and the satellite imagery in Google Earth, and neither lineaments in 2D nor plane elements in 3D could therefrom be mapped correctly regarding their orientations. Considering, though, the advantage of high resolution, Google Earth Pro was used to assist in the identification of structures via color contrasts to map them in a geometrically correct way in FaultTrace. Also, mosaicked satellite images in Google Earth could be misleading, as they usually appear with slight color variations. If mosaic tiles are draped on DEM with highly variable topographies, tile boundaries might result in color effects that resemble lithological boundaries (tile f).

In the case of the Vineh Structure and its environs, lithological units can be as thin as several meters only, and, thus, the separating bedding planes are to be mapped – if at all – only with complementary imagery from Google Earth Pro with higher resolutions. Furthermore, northwest–southeast orientated thrust faulting in the area coincides with very similar orientations of bedding planes (tiles a, c and d), hindering the color-contrast-based identification and distinction of fault from bedding planes. Therefore, only the seven most prominent faults and fracture systems (V_f1), which were to be located via the cross-section along the KWCT, are shown as fault plane elements (tiles c and d). Fault plane element 22 is the Purkan-Vardij Fault striking northwest–southeast and intersecting the KWCT in its main curve with an angle of 65–70° from the horizontal (V_I1). Further eastwards of the Vineh Structure, faults become more visible; thrust planes remain, however, difficult to identify. The east–west striking fault system of the North Tehran Fault (V_F2) is located further southeast from the Vineh Structure and not mapped. Joint sets (V_f2) reported throughout the tunnel walls speak for a heavily sheared structural geological setting but could not be mapped either due to resolution issues or a lack of color and/or morphology contrast.

For areas where thicknesses of lithological units exceed several tens of meters, bedding planes could be mapped with reasonable certainty – such as, for instance, close to the Anticline of Vardij (V_B2) encountering the KWCT just south of its main curve. In contrast, areas with almost horizontal bedding planes often lack outcrops, and correct bedding plane orientations can become difficult to measure. In this case, particular attention should be paid on falsifying shadow or other optical effects resulting, for instance, from erosion processes. An example of almost flat bedding planes is the bedding plane element 2 with an azimuth of 45° and a dip of only 2°. We assume that the topographic depression south of the Amir-Kabir Dam corresponds to the Syncline of Azgilak (V_B1); the exact location could, however, not be determined since the syncline was named after a fruit ("azgil" – Persian for: medlar).

5. Discussion

At this stage, the main focus lies in the discussion of the functionality of the tool FaultTrace. Here, the two specific geological structures served as benchmarks, as they have been extensively mapped and assessed beforehand by different authors (Table 2, Table 3). It should be noted that

both case studies were chosen expecting possibly unfavorable conditions in order to become aware of limits and room for improvement of FaultTrace.

In principle, the usage of satellite imagery draped on a DEM is optional. However, it significantly improves the correct assessment of those rock formations, which, for instance, do not show a prominent morphologic response to erosion in the DEM. Both case studies have illustrated that the accuracy of both types of data are equally important and should have similar resolution ranges (Table 1). In our case studies, resolution concerns were met by using the ALOS World 3D DEM (for the Richât Structure; 30 m) and the ALOS PALSAR DEM (for the Vineh Structure; 12.5 m) combined with Sentinel-2 (10 m) and Landsat ETM+ Imagery (30 m). Nonetheless, and even if DEM and satellite imagery resolutions match each other, certain structural geological features could not be remapped in the two case studies: (i) carbonatite dykes in the southern part of the Richât Structure and gabbro dykes in its northern part were too short and thin to appear as color contrast on satellite imagery due to resolution issues; (ii) faults parallel or subparallel to the dominant bedding sequences within the Vineh Structure were likewise non-detectable because of lacking contrast and resolution.

The importance of matching resolutions was exemplified during the comparative mapping of the Vineh Structure with Google Earth Pro. DEM with a significantly lower accuracy compared to the thereupon draped satellite imagery can result in severe distortions.

Regarding the impossibility of mapping faults or bedding planes, which are usually smaller than the resolution of the used DEM and satellite imagery, it should be considered that FaultTrace can visualize additional information such as borehole data and geological or seismic profiles supporting the mapping process. Moreover, datasets with finer resolutions could be used locally if available.

Particular attention should be paid to the vertical accuracy while mapping. In our study, both the ALOS World 3D and the ALOS PALSR DEM had vertical errors of about 5 m, which is relatively small compared to other DEM such as, for instance, SRTM DEM with 16 m. However, it should be noted that in general large vertical errors can cause considerably wrong dips – especially when mapped lineaments are short and associated plane elements are orientated only with a small closely spaced number of trace points. Hence, difficulties in positioning bedding (or fault) plane elements result not only from a small number of available outcrops representing the plane of interest but also from the vertical accuracy with respect to the altitude range of the investigated area (i.e., the signal-to-noise-ratio), which can influence the positioning in 3D considerably. Exemplarily, Figure 6a–c show a simulated noise increase and its effect on a trace line; the lower the signal-to-noise-ratio, the more frayed appears the trace line, and the higher is the inaccuracy of the respective plane element orientation measurement. Tile d serves as reference for the traced geological layer.

The vertical accuracy is likewise of particular importance when applying the three-point-method (Figure 3) in a geological setting with low dip angles. By placing points manually in a low-resolution DEM, the same altitude might be assigned to two or more points. A low signal-to-noise-ratio can result in a reversal of strike and dip directions. Particularly on mountain ridges without local topographic depressions, the mapping of collinear point sequences can be problematic, as the results will have undefined dip values.

By themselves, lineaments are "line-like" structures across a surface, which do not depend on any vertical component. If, however, lineaments are seen as intersections of a DEM and plane elements with precisely orientated strikes and dips – i.e., as trace lines –, the vertical accuracy of the DEM becomes crucial. In this context, difficulties arose at the Richât Structure while mapping almost horizontal and particularly flat bedding planes with dips of a few degrees only (Figure 7a). Similarly, the Syncline of Azgilak (assumed) north of the Vineh Structure was characterized by a bedding plane with a very low dip (Figure 7b). Here, plane element orientations are unable to be measured due to non-outcropping bedding planes in the area.

As mentioned before, the objective of this study was to test the functionality of FaultTrace instead of providing a new structural geological assessment of the Richât and the Vineh Structures. Generally speaking, the results of the virtual mapping were in very good accordance with what the available literature (Table 2, Table 3) provided. All major structural geological features such as prominent shapes, dykes, faults and fault systems, con-

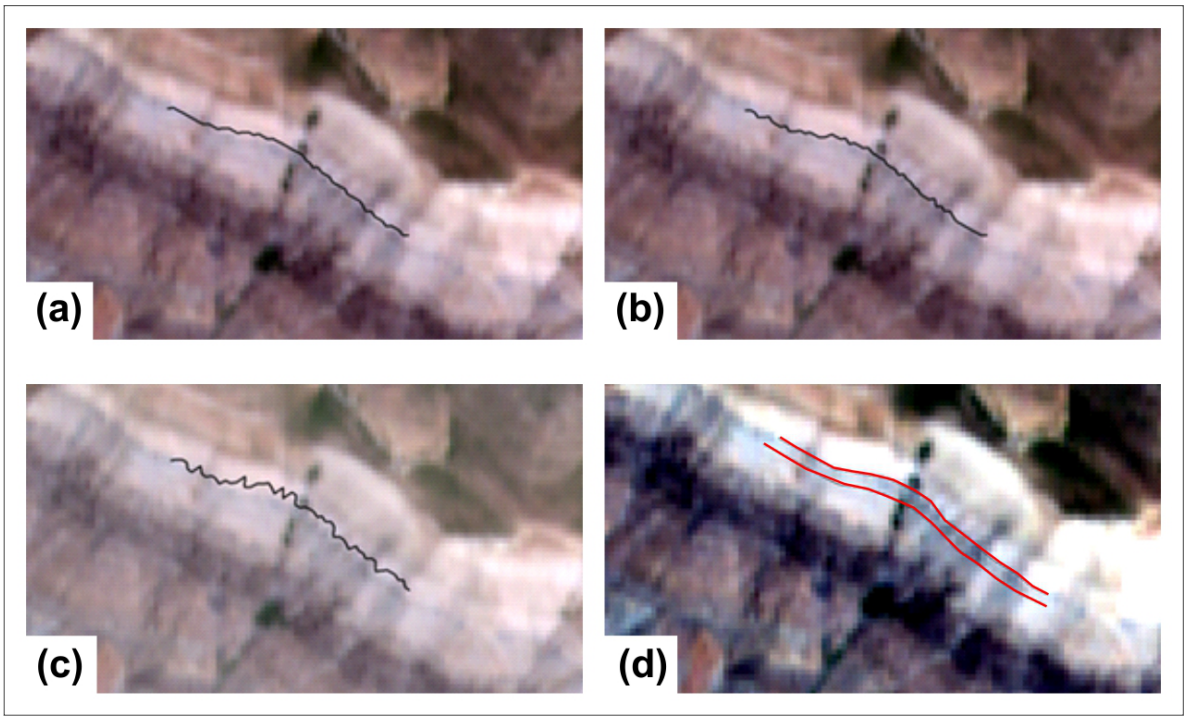

Figure 6. Influence of the signal-to-noise-ratio on the quality and appearance of a trace line on an original DEM in high resolution (a), on a DEM with added random noise (i.e., 5% of the absolute altitude range; b), and on a DEM with added random noise (i.e., 12.5% of the absolute altitude range; c). The signal-to-noise-ratio of the third tile (c) is typical for the Richât Structure. The last tile (d) shows the respective bedding boundaries (of which the northern one corresponds to the trace line) on a contrast-enhanced satellite image. The depicted structure is located at 35° 52'48.00"N, 51° 07'15.60"E east of the Vineh Structure.

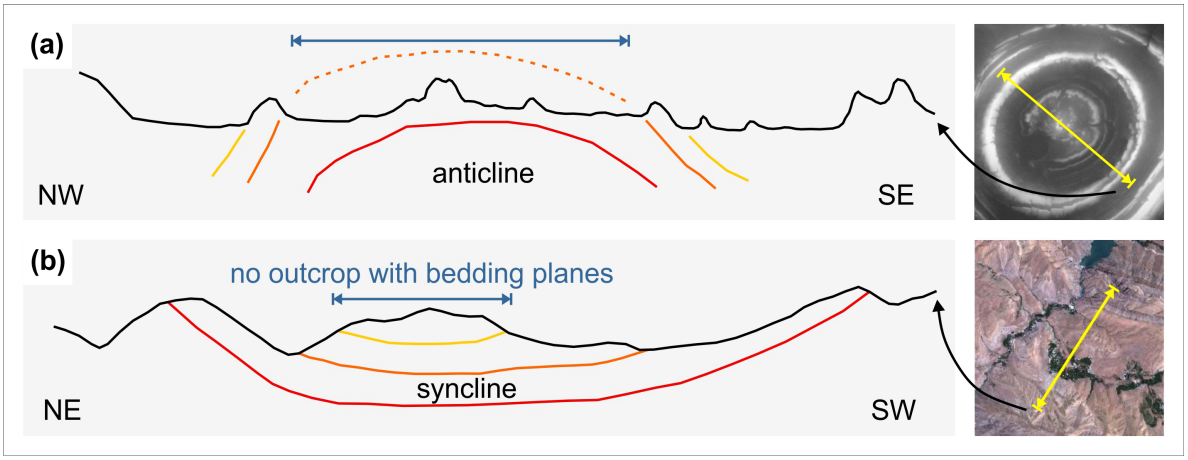

Figure 7. Lack of outcrops with bedding boundaries at the example of an anticline in the center of the Richât Structure (a) and the Syncline of Azgilak (assumed) north of the Vineh Structure (b). Both cross-sections are schematic; the vertical axis of the Richât Structure is ten-fold exaggerated.

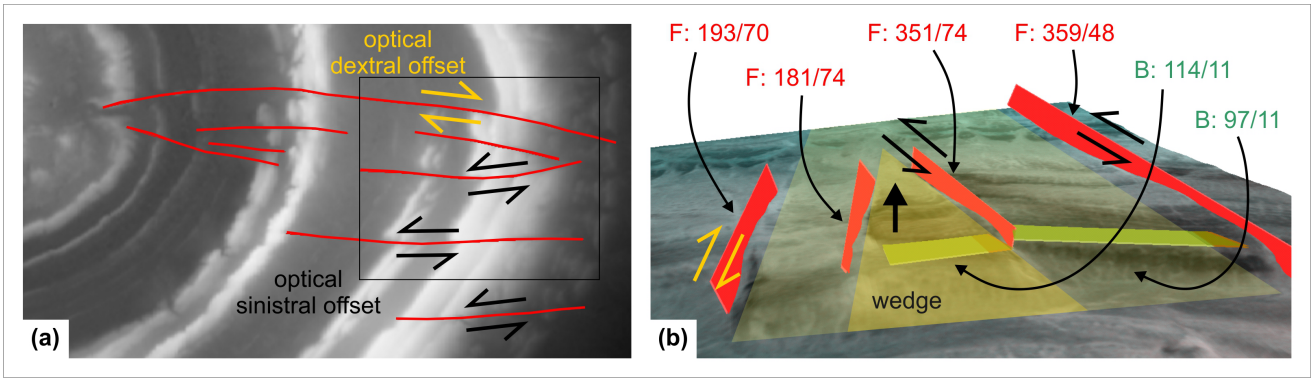

Figure 8. Examples of optical sinistral and dextral offset within the Richât Structure (a) due to vertical wedge extrusion within an environment of almost horizontal bedding (b).

jugated fracture sets, typical volcanic discordances, and bedding sequences could be identified remotely via FaultTrace. Solely the brittle fracture system in the east of the Richât Structure (Figure 4a–c; R_f2) might be addressed as the last point of discussion. It is parallel to the second fault system striking with 70–90° and reported to be sinistral by *Matton* [2008] and *Matton et al.* [2005]. With FaultTrace, however, we believe in having identified sinistral and dextral offsets within that zone (Figure 8a–b). One explanation could be a local setting of vertical wedge extrusion (i.e., so-called "flower structures") within an environment of almost horizontal bedding, which lets some of the dominant vertical offsets appear sinistral and dextral from above.

6. Conclusion

Based on two different case studies – i.e., the Richât Structure in Mauritania within a relief of low variability, and the Vineh Structure in Iran with a highly variable relief –, we have demonstrated the performance of the semi-automatic structural geological mapping tool FaultTrace of the software WinGeol.

Generally, results are satisfying, as most structural geological features – i.e., primarily faults and bedding planes – mentioned in the literature can be easily remapped with FaultTrace using satellite imagery draped on a DEM. Moreover, FaultTrace has demonstrated to be useful in rapid mapping of lineaments in 2D across a wide area, their conversion into plane elements in 3D, and the positional adjustment and intersection of the latter with the DEM. A particular asset of FaultTrace is the procedure of automatic interpolation between orientated plane elements; gaps in structural geological assessments can, thus, be filled or recovered.

Despite the potential of assistance in structural geological mapping, it is essential to note that FaultTrace does not replace field campaigns, whose level of detail cannot be achieved even with DEM or satellite data of the highest precision. Nevertheless, FaultTrace can be complementary to field campaigns during their preparation, monitoring, and/or the post-processing of collected data. In some particular cases, though, it can also serve as a self-contained tool substituting field campaigns if the terrain of interest is inaccessible, for instance, due to transportation, political restrictions, warfare, natural hazards, or lack of funding.

Author Contributions

R. F. is the developer of the software WinGeol including the tool FaultTrace; he retrieved and prepared the data, and carried out the mapping and analysis. G. D. provided the literature reviews and the therefrom retrieved data to be mapped with the new software; she wrote the publication. Conception, argumentation, data interpretation, discussion and graphic imagery are provided by both authors.

Data, Imagery and Software Sources

The data and imagery used for this publication are freely available by the following providers:

- ALOS PALSAR / Credit: EORC (JAXA) and JAROS [https://search.asf.alaska.edu/]
- ALOS World 3D / Credit: EORC (JAXA) [https://www.eorc.jaxa.jp/ALOS/en/aw3d30/index.htm]
- Landsat ETM+ / Credit: NASA and USGS [https://earthexplorer.usgs.gov/]
- Sentinel-2 Imagery / Credit: ESA [https://earthexplorer.usgs.gov/]
- various satellite images / Credit: Google Earth Pro (version 7.3.3)

The software WinGeol/FaultTrace™ is a commercial product of the company TerraMath [http://www.terramath.com/].

Acknowledgments. We express our acknowledgments to Dr. S. Sadeghi of the Department of Geology of the Imam Khomeini International University in Tehran, Iran, for having drawn our attention to the interesting geological structures close to Vineh, and for having shared with us digital cartographic work of the area which served as a detailed reference during the software test.

References

Abdullah, A., S. Nassr, A. Ghaleeb (2013), Remote Sensing and Geographic Information System for Fault Segments Mapping a Study from Taiz Area, *Journal of Geological Research*, *2013,* No. 201757, 16, **Crossref**

Akram, M. S., K. Mirza, M. Zeeshan, I. Ali (2019), Correlation of Tectonics with Geologic Lineaments Interpreted from Remote Sensing Data for Kandiah Valley, Khyber-Pakhtunkhwa, *Journal of the Geological Society of India*, *93,* 607–613, **Crossref**

Alganci, U., B. Besol, E. Sertel (2018), Accuracy Assessment of Different Digital Surface Models. International Society for Photogrammetry and Remote Sensing, *International Journal of Geo-Information*, *7,* No. 114, 16, **Crossref**

Alshayef, M. S., A. M. Mohammed, A. Javed, et al. (2017), Manual and Automatic Extraction of Lineaments From Multispectral Image in Part of Al-Rawdah, Shabwah, Yemen by Using Remote Sensing and GIS Technology, *International Journal of New Technology and Research*, *3,* No. 2, 67–73.

Allmendinger, R. W. (2018), *A Structural Geology Laboratory Manual for the 21st Century, v.1.8.0*, 325 pp. Cornell University – Engineering Earth and Atmospheric Sciences, College of Agriculture and Life Sciences, Ithaca, New York.

Bagheri, A., A. Asgary, J. Levy, M. Rafieian (2006), A Performance Index for Assessing Urban Water Systems: A Fuzzy Inference Approach, *Journal of the American Water Works Association*, *98,* No. 11, 84–92, **Crossref**

Barringer, R. W. (1967), World's Meteorite Craters "Astroblemes", *Meteoritics and Planetary Science*, *3,* No. 3, 151–157, **Crossref**

Bayik, C., K. Becek, C. Mekik, M. Ozendi (2018), On the Vertical Accuracy of the ALOS World 3D-30m Digital Elevation Model, *Remote Sensing Letters*, *9,* No. 6, 607–615, **Crossref**

Cailleux, A., A. Guillemaut, C. Pomerol (1964), Présence de Coésite, Indice de Hautes Pressions, dans l'Accident Circulaire des Richat, *Comptes Rendus de l'Académie des Sciences*, *258,* 5488–5490.

Chu, T., K. E. Lindenschmidt (2017), Comparison and Validation of Digital Elevation Models Derived from InSAR for a Flat Inland Delta in the High Latitudes of Northern Canada, *Canadian Journal of Remote Sensing*, *43,* No. 2, 109–123, **Crossref**

Deynoux, M., R. Trompette (1971), La Série Stratigraphique des Richat; Comparaison avec l'Adrar de Mauritanie (Sahara occidental), *Bulletin de la Société Géologique de France*, *S7-XIII,* No. 1–2, 111–117, **Crossref**

Dietz, R., R. Fudali, W. Cassidy, et al. (1969), Richat and Semsiyat Domes (Mauritania): Not Astroblemes, *Geological Society of America Bulletin*, *80,* No. 7, 1367–1372, **Crossref**

Elhag, M., D. Alshamsi (2019), Integration of Remote Sensing and Geographic Information Systems for Geological Fault Detection on the Island of Crete, Greece, *Geoscientific Instrumentation, Methods and Data Systems*, *8,* 45–54, **Crossref**

Elkhrachy, I. (2019), Vertical Accuracy Assessment for SRTM and ASTER Digital Elevation Models: A Case Study of Najran City, Saudi Arabia, *Ain Shams Engineering Journal*, *9,* No. 4, 1807–1817, **Crossref**

Faber, R., G. Domej (2020), Computer-Assisted Geological Mapping (CAGEM) in 3D with WinGeol by TerraMath: the Richât Structure in Mauritania, Geophysical Research Abstracts, vol. 22 (EGU2020–2439), p. 1, European Geoscience Union General Assembly, Vienna, Austria. **Crossref**

Farhadian, H., H. Katibeh, P. Huggenberger, et al. (2016), Empirical Model for Estimating Groundwater Flow into Tunnel in Discontinuous Rock Masses, *Environmental Earth Sciences*, *74,* No. 471, 16, **Crossref**

Farhadian, H., A. Nikvar-Hassani, H. Katibeh (2017), Groundwater Inflow Assessment to Karaj Water Con-

veyance Tunnel, Northern Iran, *Korean Society of Civil Engineers Journal*, *21,* No. 6, 2429–2438, **Crossref**

Farr, T.G., P.A. Rosen, E. Caro, et al. (2007), The Shuttle Radar Topography Mission, *Reviews of Geophysics*, *45,* No. 2, 33, **Crossref**

Fudali, R.F. (1969), Coesite from the Richat Dome, Mauritania: A Misidentification, *Science*, *166,* No. 3902, 228–230, **Crossref**

Ghiasi, V., S. Ghiasi, A. Prasad (2012), Evaluation of Tunnels Under Squeezing Rock Condition, *Journal of Engineering, Design and Technology*, *10,* No. 2, 168–179, **Crossref**

Gupta, R. P. (2003), Evaluation of Tunnels Under Squeezing Rock Condition, *Journal of Engineering, Design and Technology*, 656, **Crossref**

Hassanpour, J., J. Rostami, M. Khamehchiyan, et al. (2010), TBM Performance Analysis in Pyroclastic Rocks: A Case History of Karaj Water Conveyance Tunnel, *Rock Mechanics and Rock Engineering*, *43,* 427–445, **Crossref**

Hassanpour, J., J. Rostami, S. Tarigh-Azali, J. Zhao (2014), Introduction of an Empirical TBM Cutter Wear Prediction Model for Pyroclastic and Mafic Igneous Rocks; a Case History of Karaj Water Conveyance Tunnel, Iran, *Tunnelling and Underground Space Technology*, *43,* 222–231, **Crossref**

Jalali, M. (2018), Tunnel Rehabilitation in Fault Zone Using Sequential Joints Method- Case Study: Karaj Water Conveyance Tunnel, *International Journal of Mining and Geo-Engineering*, *52,* No. 1, 87–94, **Crossref**

Janda, C., R. Faber, C. Hager, B. Grasemann, et al. (2003), Automatic Fault Tracing of Active Faults in the Sutlej Valley (NW-Himalayas, India), Geophysical Research Abstracts vol. 5(10334), p. 1, European Geophysical Society, Vienna, Austria.

Julzarika, A. (2015), Height Model Integration of ALOS PALSAR, X SAR, SRTM C and ICESAT/GLAS, *International Journal of Remote Sensing and Earth Sciences*, *12,* No. 2, 107–116, **Crossref**

Karamouz, M., B. Zahraie, S. Araghi–Nejhad, et al. (2001), An Integrated Approach to Water Resources Development of the Tehran Region in Iran, *Journal of the American Water Resources Association*, *37,* No. 5, 1301–1211, **Crossref**

Khanlari, G., R. Ghaderi-Meybodi (2011), Analysis of Rock Burst in Critical Section of Second Part of Karaj-Tehran Water Supply Tunnel, Geotechnical Safety and Risk, p. 661–668, Proceedings of the 3rd International Symposium on Geotechnical Safety and Risk, Munich, Germany.

Khanlari, G., R. Ghaderi-Meybodi (2013), Evaluation of Rockburst Potential in Second Part of Karaj–Tehran Water Conveyance Tunnel, *Journal of Engineering Geology*, *6,* No. 2, 1545–1558.

Khanlari, G., R. Ghaderi-Meybodi, E. Mokhtari (2012), Engineering Geological Study of the Second Part of Water Supply Karaj to Tehran Tunnel with Emphasis on Squeezing Problems, *Engineering Geology*, *145–146,* 9–17, **Crossref**

Matton, G. (2008), Le Complèxe Crétacé du Richât (Mauritanie); un Processus Alcalin Péri-Atlantique, Geotechnical Safety and Risk, p. 172, University of Québec, Chicoutimi, Canada. **Crossref**

Matton, G., M. Jébrak (2014), The "Eye of Africa" (Richat dome, Mauritania): An Isolated Cretaceous Alkaline-Hydrothermal Complex, *Journal of African Earth Sciences*, *97,* 109–124, **Crossref**

Matton, G., M. Jébrak, J. K. W. Lee (2005), Resolving the Richat Enigma: Doming and Hydrothermal Karstification Above an Alkaline Complex, *Geology*, *33,* No. 8, 665–668, **Crossref**

Master, S., J. Karfunkel (2001), An Alternative Origin for Coesite from the Richat Structure, Mauritania, *Meteoritics and Planetary Science*, *36,* No. 9/Supplement, A125.

Mirahmadi, M., M. Tabaei, M. Soleiman-Dehkordi (2016), Studying the Effect of Tunnel Depth Variation on the Specific Energy of TBM, Case Study: Karaj-Tehran (Iran) Water Conveyance Tunnel, *Journal of Engineering and Technological Sciences*, *48,* No. 4, 408–416, **Crossref**

Monod, T. (1965), *Contribution à l'Établissement d'une Liste d'Accidents Circulaires d'Origine Météoritique (Reconnue, Possible ou Supposée), Cryptoexplosive, etc., Ed. 2 (Catalogue XVIII)*, 93 pp. Institut Fondamental d'Afrique Noire, Dakar, Senegal.

Morsali, M., M. Nakhaei, M. Rezaei, et al. (2017), A New Approach to Water Head Estimation Based on Wwater Inflow Into the Tunnel (Case Study: Karaj Water Conveyance Tunnel), *Quarterly Journal of Engineering Geology and Hydrogeology*, *50,* No. 2, 126–132, **Crossref**

Morsali, M., M. Nakhaei, M. Rezaei, et al. (2018), The Comparison of Effective Variables and Methods in Water Inflow into Hard Rock Tunnels (Case Study: Karaj Dam – Tehran Water Conveyance Tunnel), *Scientific Quarterly Journal / Geosciences*, *27,* No. 107, 113–122, **Crossref**

Mukul, M., V Srivastava, S. Jade (2017), Uncertainties in the Shuttle Radar Topography Mission (SRTM) Heights: Insights from the Indian Himalaya and Peninsula, *Scientific Reports*, *7,* No. 41672, 10, **Crossref**

Netto, A. M., J. Fabre, G. Poupeau, M. Champenois (1992), Datation Par Traces de Fission de la Structure Circulaire des Richat (Mauritanie), *Comptes Rendus de l'Académie des Sciences*, *314,* No. 11, 1179–1186.

O'Leary, D. W., J. D. Friedman, H. A. Pohn (1976), Lineament, Linear, Lineation: Some Proposed New Standards for Old Terms, *Geological Society of America Bulletin*, *87,* No. 10, 1463–1469, **Crossref**

Poupeau, G., J. Fabre, E. Labrin, et al. (1996), Nouvelles Datations par Traces de Fission de la Structure Circulaire des Richat (Mauritanie), *Mémoire du*

Service Géologique de l'Algérie, *8,* 231–236, **Crossref**

Rajabi, S., M. Eliassi, A. Saidi (2012), Statistic and Genetic Investigation of Faults in North Tehran Tectonic Wedge (South Central Alborz), *Arabian Journal of Geosciences*, *5,* 1269–1277, **Crossref**

Reif, D., B. Grasemann, R. Faber (2011), Quantitative Structural Analysis Using Remote Sensing Data: Kurdistan, Northeast Iraq, *Bulletin of the American Association of Petroleum Geologists*, *95,* No. 6, 941–956, **Crossref**

Richard-Molard, J. (1948), La Boutonnière du Richât en Adrar Mauritanien, *Comptes Rendus de l'Académie des Sciences*, *227,* 142–143.

Rodrigues, T. G., W. R. Paradella, C. G. Oliveira (2011), Evaluation of the Altimetry from SRTM-3 and Planimetry from High-Resolution PALSAR FBD Data for Semi-Detailed Topographic Mapping in the Amazon Region, *Anais da Academia Brasileira de Ciências*, *83,* No. 3, 953–966, **Crossref**

Santillan, J. R., M. Makinano-Santillan (2016), Vertical Accuracy Assessment of 30-M Resolution Alos, Aster, and Srtm Global Dems Over Northeastern Mindanao, Philippines, *International Archives of the Photogrammetry, Remote Sensing and Spatial Information Sciences*, *XLI,* No. B4, 149–156, **Crossref**

Sao, O., P. Giresse, et al. (2008), Les Environnements Sédimentaires des Gisements Pré-acheuléens et Acheuléens des Wadis Akerdil et Bamouéré (Guelb er-Richât, Adrar, Mauritanie), une Première Approche, *L'Anthropologie*, *112,* No. 1, 1–14, **Crossref**

Scheffers, A. M., S. M. May, D. H. Kelletat (2015), Tectonic Landforms, *L'Anthropologie*, 75–120, **Crossref**

Shawky, M., A. Moussa, Q. K. Hassan, N. El-Sheimy (2019), Pixel-Based Geometric Assessment of Channel Networks/Orders Derived from Global Spaceborne Digital Elevation Models, *Remote Sensing*, *11,* No. 3, 33, **Crossref**

Soleiman-Dehkordi , M., H. A. Lazemi, K. Shahriar (2015), Application of the Strain Energy Ratio and the Equivalent Thrust per Cutter to Predict the Penetration Rate of TBM, Case Study: Karaj-Tehran Water Conveyance Tunnel of Iran, *Arabian Journal of Geosciences*, *8,* 4833–4842, **Crossref**

Spitzbart, A. (1960), A Generalization of Hermite's Interpolation Formula, *The American Mathematical Monthly*, *67,* No. 1, 42–46, **Crossref**

Venegas, G., J. Martínez-Frías, et al. (2012), Proceedings of the 10-th International GeoRaman Conference, Raman Spectroscopic Mineralogical Characterisation of Richat structure (Mauritania), p. 273–274, GeoRaman Conference, Nancy, France.

Woolley, A. R. (2001), *Alkaline Rocks and Carbonatites of the World – Part 3 – Africa*, 372 pp. The Geological Society of London, London, England.

Corresponding author:

G. Domej, Università degli Studi di Milano-Bicocca, Dipartimento di Scienze dell'Ambiente e della Terra, Piazza della Scienza 1/U4, 20126 Milano, Italy. (gisela.domej@unimib.it)